Journal of
Marine Science and Engineering

MDPI

Article

Short-Crested Wave–Current Forces on a Concentric System with an ARC Exterior Porous Wall

Jianming Miao [1], Dan Liu [2], Jie Li [1] and Zhenfeng Zhai [3,*]

[1] School of Ocean Engineering and Technology, Sun Yat-Sen University, and Southern Marine Science and Engineering Guangdong Laboratory (Zhuhai), Zhuhai 519000, China
[2] Department of Mechanical and Structural Engineering and Materials Science, University of Stavanger, N-4036 Stavanger, Norway
[3] School of Intelligent Systems Engineeing, Sun Yat-Sen University, Shenzhen 518000, China
* Correspondence: zhaizhf3@mail.sysu.edu.cn

Abstract: In this study, the potential flow theory is adopted to develop an analytical solution to the diffraction problem of a short-crested wave–current incident on a concentric system consisted of an arc exterior wall and interior cylinder. The influence of the uniform current on the hydrodynamic performance of the concentric structure is primarily discussed. The incident angle and speed of the uniform current significantly influence the short-crested wave force and run-up on the concentric structure. Specific parametric conditions are obtained, under which the wave structure can resonate, and the resonance phenomenon may be more pronounced when the wave and current have the same incidence direction. Furthermore, semi-enclosed structures are highly sensitive to the direction of wave incidence, thereby triggering certain limitations in engineering applications. This study is expected to contribute as theoretical guidance to nearshore architecture designs.

Keywords: wave–structure interactions; short-crested wave–current; wave diffraction; arc-shaped structure

Citation: Miao, J.; Liu, D.; Li, J.; Zhai, Z. Short-Crested Wave–Current Forces on a Concentric System with an ARC Exterior Porous Wall. *J. Mar. Sci. Eng.* **2023**, *11*, 573. https://doi.org/10.3390/jmse11030573

Academic Editor: Alessandro Antonini

Received: 23 January 2023
Revised: 20 February 2023
Accepted: 21 February 2023
Published: 7 March 2023

1. Introduction

Investigating the effects of ocean waves on coastal structures is a crucial topic for marine engineering. Significant wave loading and run-up occur when waves directly impact these marine structures, thereby triggering structure overturning and wave overtopping. In practical engineering, permeable layers are often built around offshore structures to protect them from the direct impact of waves because porous structures can reduce wave height to protect coastal structures from erosion and minimize wave forces by dissipating and partially reflecting incident wave energy. Hence, concentric porous structures are widely used in offshore engineering. There structures generally comprise permeable external and impermeable internal structures, for example, the Ekofisk gravity offshore structure in the North Sea [1]. Consequently, researchers in coastal/ocean engineering have conducted several studies on the phenomenon of waves cutting through a permeable structure.

Chwang [2] proposed a linearized porous-wavemaker theory, which was first applied in the analysis of amplitude surface waves aroused by permeable vertical plate horizontally oscillating motion. Then, the surface waves aroused by a piston-type porous wavemaker close to the end of a semi-infinitely long channel in constant water depth were later analyzed using the theory [3]. A theoretical study of the interaction between regular waves and and a perforated cylinder with the same axis was conducted relatively early by Wang and Ren [4]. They deduced that the wave elevation and wave load decrease with an increase in the porosity coefficient of the outer column of a double-column cylinder. Subsequently, numerous scholars have studied the interaction of waves with individual peer columns by employing different wave theories, such as Airy [5–9], short-crested [1,10], and shallow water [11,12] wave theories. Considering a series of surface-penetrating, bottom-mounted,

perforated cylinders with permeable exterior walls, various structural parameters and wave effects were discussed by Sankarbabu et al. [13]. Zhao et al. [14] conducted research on the interaction between waves and a submerged porous bar protecting a vertical wall that can reflect waves in part; accordingly, they determined that the wave resonance disappears when the vertical wall has a small reflection coefficient. Zhai et al. [15–17] investigated the diffraction of water waves by a concentric dual-arc breakwater using a theoretical method. From the interaction results between regular waves and permeable systems with the same axis, whose smooth sections can be arbitrary, Liu et al. [18] determined a solution to the problem. The interaction between the linear wave and truncated partially permeable cylinders of finite water depth was addressed by Sarkar and Bora [19], who compared the results of floating and bottom-supported combined systems. The obtained results demonstrate that the values of the radii should be larger than 0.15 to achieve smaller forces and less resonance. The theoretical, numerical, and experimental studies conducted by various scholars provide a deep understanding of concentric cylindrical systems, which has laid the foundation for their practical engineering applications. Based on linear potential flow theory and an eigenfunction expansion method, Zheng et al. [20–22] studied wave scattering by an array of circular floating porous elastic plates, submerged porous elastic disks, and a floating porous elastic plate of arbitrary shape, respectively. Cuong and Tuan [23] present a laboratory study on wave transmission across steep platform reefs and establish empirical formulations of spectral wave parameters across the reef flat. Kamil et al. [24] discuss the attenuation mechanism of mangroves and the factors influencing the dissipation performance.

In actual marine environments, when the wind blows across the water surface, short-crested waves are produced. Short-crested waves have limited lateral extent and significantly differ from long-crested plane waves in their characteristics. Zhu [25] conducted a study on the diffraction of short-crested waves in a solid cylinder, and the obtained results indicate that the hydrodynamic forces triggered by short-crested waves on an impermeable cylinder are consistently smaller than the hydrodynamic forces caused by plane waves with the same total wave number. Based on the scaled boundary finite element method, Liu et al. [26] numerically studied short-crested wave diffraction by combining an exterior arc-shaped porous cylinder encircling and an interior impermeable cylinder. Zhai et al. [27] studied the interaction between short-crested wave and V- and arc-shaped breakwaters and then compared the hydrodynamic properties of the V- and arc-shaped breakwaters.

Currently, ocean current load is crucial in the actual ocean and substantially influences wave conditions. The coexistence of waves and currents is a prevalent phenomenon in most ocean environments. Relatively weak currents can potentially alter the wavelength, amplitude, propagation direction, and power spectral density of gravity waves. For strong currents, the effects of wave–current interactions are more significant. The coupling between wave and current is common in actual ocean environments. Lin and Li [28] studied the interaction between wave–current and a vertical square cylinder and deduced that the strength and frequency of vortex shedding induced by a uniform current can be reduced by the presence of waves. Jian et al. [29] investigated the short-crested wave–current forces encircling a large vertical circular cylinder considering the influence of uniform currents. The obtained results indicate that when the current speed increases even with low growth, the run-up, loads, pressure, and crest profiles of waves surpass wave cases without current for both long- and short-crested waves. Wang et al. [30] derived an analytical solution for the short-crested wave with uniform current diffraction on a composite bucket foundation for an offshore wind turbine. Zhou and Zhou [31] established a numerical simulation model suitable for wave–current interaction on the Submerged Dike Terrain, comparing it with other analytical solutions and physical model experiment results, thus demonstrating that the model can effectively simulate wave propagation and deformation under different current environments. Huang et al. [32] proposed a frequency-domain numerical model to study the hydrodynamic performances of various three-dimensional bodies under the effect of waves and weak current in a channel according to the higher-order boundary element

method. Zhou et al. [33] presented the characteristics of the heave motion responses and wave forces of a horizontal floating cylinder during a wave–current interaction.

This investigation includes the short-crested wave–current forces on a combined structure comprising an arc out wall and interior cylinder. An analytical solution is derived for the diffraction between short-crested incident waves with uniform current and the structure. The effects of the speed and angle of incidence of current, porous-effect parameter, short-crestedness, location of the arc wall on the hydrodynamic force, wave run-up, and diffracted wave contours are examined. The obtained results can provide helpful guidance for the offshore structure engineering design and exploitation.

2. Formulation

The geometry of the problem is illustrated in Figure 1, in which the Cartesian $O-xyz$ and cylindrical $O-r\theta z$ coordinate systems are employed, and the z-axis points are vertically upward from the flat seabed. The symbols h, a, and b denote the water depth, radii of the arc wall, and interior cylinder, respectively. The central angles of the arc wall are denoted as γ. In addition, α denotes the angle between the positive axis of the x-axis of the arc wall and one end. Hence, γ and α can be adopted consistently to determine the positions of the arc wall. The fluid region can be divided into two parts according to a virtual interface: outside $\Omega_1(r \geq a)$ and inside $\Omega_2(b \leq r \leq a)$ regions. Assume that the fluid is homogeneous, incompressible, inviscid, and irrotational in flow. The velocity potential is expressed as $\Phi(x,y,z,t) = \mathrm{Re}[\phi(x,y,z,t)]$, where ϕ denotes the complex potential. Furthermore, $\phi^{(j)} = \phi_I + \phi_S^{(j)} (j = 1,2)$ (ϕ_I and $\phi_S^{(j)}$ denote the complex incident and scattered potential, respectively), where $\phi^{(1)}$ is the complex velocity potential in the exterior region Ω_1, and $\phi^{(2)}$ is complex velocity potential in the interior region Ω_2. In the two sub-regions, the complex potentials $\phi^{(j)}$ satisfy the Laplace equation:

$$\nabla^2\phi^{(1)} = \nabla^2\phi^{(2)} = 0 \tag{1}$$

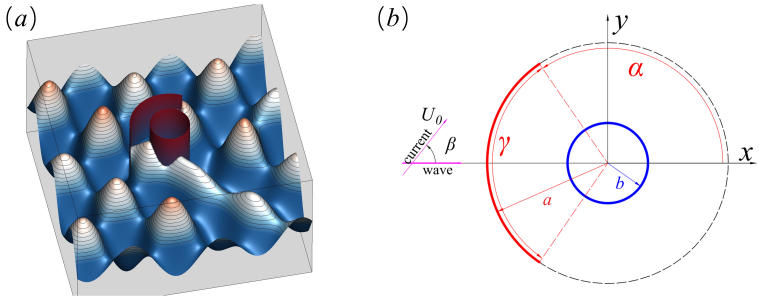

Figure 1. Definition sketch: (**a**) bird's-eye view; (**b**) top view.

To calculate the velocity potential for short-crested incident waves traveling in the positive x-direction with uniform current, the real part is expressed in accordance with the following form [25,30]:

$$\begin{aligned}\phi_I &= -\mathrm{i}\frac{gH\cosh(kz)}{2\omega^*\cosh(kh)}e^{\mathrm{i}(k_x x-\omega t)}\cos(k_y y)\\ &= -\mathrm{i}\frac{gH\cosh(kz)}{2\omega^*\cosh(kh)}e^{-\mathrm{i}\omega t}\sum_{n=0}^{\infty}\varepsilon_n \mathrm{J}_n(kr)\cos(n\theta)\cos(n\chi)\end{aligned} \tag{2}$$

where ω^* is the incident wave frequency relative to a reference system with uniform current U_0. g is the gravitational acceleration, H is the wave height, and ω is the angular wave frequency. k_x and k_y denote the wave numbers in the x- and y-directions, respectively, and $k = \sqrt{k_x^2 + k_y^2}$ denotes the total wave number that satisfies the dispersion relation $\omega^2 = gk\tanh(kh)$. $\varepsilon_0 = 1$ and $\varepsilon_n = 2\mathrm{i}^n$ for $n \geq 1$. $\mathrm{J}_n(\cdot)$ denotes the n-th order Bessel

function of the first type. When uniform current exists, the wave frequency can be expressed as $(\omega - \overrightarrow{k} \cdot \overrightarrow{U_0})^2 = (\omega^*)^2 = gk\tanh(kh)$, where $\overrightarrow{k} = (k_x, k_y)$, $\overrightarrow{U_0} = |\overrightarrow{U_0}|(\cos(\beta), \sin(\beta))$ is the uniform current components in x-axis and y-axis directions, respectively. $\chi = \arccos(k_x/k)$ is the wave propagation direction. The short-crested waves are formed when obliquely incident plane waves reaching the offshore superimpose reflected waves from the obliquely incident plane waves. Short-crested waves have flat troughs and steep crests with a diamond-shaped waveform.

The boundary conditions on the free surface and water-bottom can be written as follows:

$$\frac{\partial \phi^{(j)}}{\partial z} = \frac{\omega^2}{g}\phi^{(j)} \quad (z = h, j = 1, 2) \tag{3}$$

$$\frac{\partial \phi^{(j)}}{\partial z} = 0 \quad (z = 0, j = 1, 2) \tag{4}$$

The boundary condition on the impermeable interior cylinder can be expressed as follows:

$$\frac{\partial \phi^{(2)}}{\partial r} = 0 \quad (r = b) \tag{5}$$

On the virtual cylinder interface, the potentials satisfy the following matching conditions:

$$\phi^{(1)} = \phi^{(2)} \ \ (r = a, \alpha + \gamma - 2\pi \le \theta \le \alpha) \tag{6}$$

$$\frac{\partial \phi^{(1)}}{\partial r} = \frac{\partial \phi^{(2)}}{\partial r} \ \ (r = a, 0 \le \theta \le 2\pi) \tag{7}$$

The boundary condition on the porous arc wall is expressed as follows:

$$\frac{\partial \phi^{(1)}}{\partial r} = \frac{\partial \phi^{(2)}}{\partial r} = \mathrm{i}kG(\phi^{(2)} - \phi^{(1)}) \quad (r = a) \tag{8}$$

where G denotes the non-dimensional porous coefficient. The factor $G = G_R + \mathrm{i}G_I$ depends on the viscosity of the fluid, the thickness of the exterior cylinder, and the porosity of the cylinder; G_R corresponds to the drag term, which will induce wave energy loss; and G_I corresponds to the inertia term, which will cause the wave motion to delay in phase after transiting over the wall of the exterior cylinder. The Sommerfeld out-going condition for scattering waves at infinity

$$\lim_{r\to\infty} \sqrt{r}[\frac{\partial \phi_s^{(1)}}{\partial r} - \mathrm{i}k\phi_s^{(1)}] = 0. \tag{9}$$

Boundary conditions in Equations (1)–(9) should be satisfied by the total velocity potential $\phi^{(j)}$ $(j = 1, 2)$ in two regions, yielding

$$\begin{aligned}\phi^{(1)} = -\mathrm{i}\frac{gH\cosh(kz)}{2\omega^*\cosh(kh)}e^{-\mathrm{i}\omega t}\sum_{n=0}^{\infty}\Big\{&\epsilon_n J_n(kr)\cos(n\theta)\cos(n\chi) \\ &+H_n^{(1)}(kr)[A_n\cos(n\theta) + B_n\sin(n\theta)]\Big\}\end{aligned} \tag{10}$$

$$\phi^{(2)} = -\mathrm{i}\frac{gH\cosh(kz)}{2\omega^*\cosh(kh)}e^{-\mathrm{i}\omega t}\sum_{n=0}^{\infty}\Big\{[C_n\cos(n\theta) + D_n\sin(n\theta)] \times [J_n(kr) - \frac{J_n'(kb)}{H_n^{(1)\prime}(kb)}H_n^{(1)}(kr)]\Big\} \tag{11}$$

where A_n, B_n,C_n, and D_n are unknown complex coefficients, and $H_n^{(1)}$ denotes the Hankel function of the first type. Substituting the velocity potentials in the two domains into the boundary Condition (7) gives

$$B_n H_n^{(1)\prime}(ka) = D_n[J_n'(ka) - \frac{J_n'(kb)}{H_n^{(1)\prime}(kb)}H_n^{(1)\prime}(ka)] \quad (n = 1, 2, 3, ...) \tag{12}$$

$$\epsilon_n \cos(n\chi) J_n'(ka) + A_n H_n^{(1)\prime}(ka) = C_n [J_n'(ka) - \frac{J_n'(kb)}{H_n^{(1)\prime}(kb)} H_n^{(1)\prime}(ka)] \quad (n = 0, 1, 2, ...) \tag{13}$$

Substituting the velocity potentials in the two domains into the boundary Conditions (6) and (8) gives:

$$\begin{aligned} f_1(\theta) = \sum_{n=0}^{\infty} \Big\{ & \epsilon_n J_n'(ka) \cos(n\theta) \cos(n\chi) + H_n^{(1)\prime}(ka) [A_n \cos(n\theta) + B_n \sin(n\theta)] \\ & - [C_n \cos(n\theta) + D_n \sin(n\theta)] \times [J_n(ka) - \frac{J_n'(kb)}{H_n^{(1)\prime}(kb)} H_n^{(1)}(ka)] \Big\} = 0 \end{aligned} \tag{14}$$

$$\begin{aligned} f_2(\theta) = & \sum_{n=0}^{\infty} \Big\{ \epsilon_n J_n'(ka) \cos(n\theta) \cos(n\chi) + \sum_{n=0}^{\infty} A_n [k H_n^{(1)\prime}(ka) + \mathrm{i}GkH_n^{(1)}(ka)] \cos(n\theta) \\ & + \sum_{n=1}^{\infty} B_n [k H_n^{(1)\prime}(ka) + \mathrm{i}GkH_n^{(1)}(ka)] \sin(n\theta) - \sum_{n=0}^{\infty} C_n \mathrm{i}Gk [J_n(ka) - \frac{J_n'(kb)}{H_n^{(1)\prime}(kb)} H_n^{(1)}(ka)] \cos(n\theta) \\ & - \sum_{n=1}^{\infty} D_n \mathrm{i}Gk [J_n(ka) - \frac{J_n'(kb)}{H_n^{(1)\prime}(kb)} H_n^{(1)}(ka)] \sin(n\theta) = 0 \end{aligned} \tag{15}$$

where the functions $f_1(\theta)$ and $f_2(\theta)$ may form a new function $F(\theta)$, yielding

$$F(\theta) = \begin{cases} f_1(\theta), \ 2\pi - \alpha - \gamma \le \theta \le \alpha \\ f_2(\theta), \ \alpha \le \theta \le \alpha + \gamma \end{cases} \tag{16}$$

In addition, the piecewise function $F(\theta)$ may be expressed as a Fourier series between $[0, 2\pi]$, i.e.,

$$F(\theta) = \frac{a_0}{2} + \sum_{m=1}^{\infty} [a_m \cos(m\theta) + b_m \sin(m\theta)] = 0 \tag{17}$$

$$\int_0^{2\pi} \cos(m\theta) F(\theta) \mathrm{d}\theta = 0, \ m = 0, 1, \cdots; \ \int_0^{2\pi} \sin(m\theta) F(\theta) \mathrm{d}\theta = 0, \ m = 1, 2, \cdots \tag{18}$$

Substituting Equations (14) and (15) into Equation (18) yields

$$\begin{aligned} & \epsilon_n \cos(m\chi) J_n(ka) I_{nm}^{(1)} + \epsilon_n [k J_n'(ka) + \mathrm{i}GkJ_n(ka)] \cos(n\lambda) I_{nm}^{(3)} + A_n H_n^{(1)\prime} I_{nm}^{(1)} + B_n H_n^{(1)\prime} I_{nm}^{(2)} \\ & + A_n [k H_n^{(1)\prime}(ka) + \mathrm{i}GkH_n^{(1)}(ka)] I_{nm}^{(3)} + B_n [k H_n^{(1)\prime}(ka) + \mathrm{i}GkH_n^{(1)}(ka)] I_{nm}^{(4)} \\ & - C_n \{ [J_n'(ka) - \frac{J_n'(kb)}{H_n^{(1)\prime}(kb)} H_n^{(1)\prime}(ka)] I_{nm}^{(1)} + \mathrm{i}Gk [J_n(ka) - \frac{J_n'(kb)}{H_n^{(1)\prime}(kb)} H_n^{(1)}(ka)] I_{nm}^{(3)} \} \\ & - D_n \{ [J_n'(ka) - \frac{J_n'(kb)}{H_n^{(1)\prime}(kb)} H_n^{(1)\prime}(ka)] I_{nm}^{(2)} + \mathrm{i}Gk [J_n(ka) - \frac{J_n'(kb)}{H_n^{(1)\prime}(kb)} H_n^{(1)}(ka)] I_{nm}^{(4)} \} = 0 \end{aligned} \tag{19}$$

$$\begin{aligned} & \epsilon_n \cos(m\chi) J_n(ka) I_{nm}^{(5)} + \epsilon_n [k J_n'(ka) + \mathrm{i}GkJ_n(ka)] \cos(n\lambda) I_{nm}^{(7)} + A_n H_n^{(1)\prime} I_{nm}^{(5)} + B_n H_n^{(1)\prime} I_{nm}^{(6)} \\ & + A_n [k H_n^{(1)\prime}(ka) + \mathrm{i}GkH_n^{(1)}(ka)] I_{nm}^{(7)} + B_n [k H_n^{(1)\prime}(ka) + \mathrm{i}GkH_n^{(1)}(ka)] I_{nm}^{(8)} \\ & - C_n \{ [J_n'(ka) - \frac{J_n'(kb)}{H_n^{(1)\prime}(kb)} H_n^{(1)\prime}(ka)] I_{nm}^{(5)} + \mathrm{i}Gk [J_n(ka) - \frac{J_n'(kb)}{H_n^{(1)\prime}(kb)} H_n^{(1)}(ka)] I_{nm}^{(7)} \} \\ & - D_n \{ [J_n'(ka) - \frac{J_n'(kb)}{H_n^{(1)\prime}(kb)} H_n^{(1)\prime}(ka)] I_{nm}^{(6)} + \mathrm{i}Gk [J_n(ka) - \frac{J_n'(kb)}{H_n^{(1)\prime}(kb)} H_n^{(1)}(ka)] I_{nm}^{(8)} \} = 0 \end{aligned} \tag{20}$$

$$\begin{cases} I_{nm}^{(1)} = \int_{\alpha+\gamma-2\pi}^{\alpha} \cos(m\theta) \cos(n\theta) \mathrm{d}\theta; & I_{nm}^{(2)} = \int_{\alpha+\gamma-2\pi}^{\alpha} \cos(m\theta) \sin(n\theta) \mathrm{d}\theta \\ I_{nm}^{(3)} = \int_{\alpha}^{\alpha+\gamma} \cos(m\theta) \cos(n\theta) \mathrm{d}\theta; & I_{nm}^{(4)} = \int_{\alpha}^{\alpha+\gamma} \cos(m\theta) \sin(n\theta) \mathrm{d}\theta \\ I_{nm}^{(5)} = \int_{\alpha+\gamma-2\pi}^{\alpha} \sin(m\theta) \cos(n\theta) \mathrm{d}\theta; & I_{nm}^{(6)} = \int_{\alpha+\gamma-2\pi}^{\alpha} \sin(m\theta) \sin(n\theta) \mathrm{d}\theta \\ I_{nm}^{(7)} = \int_{\alpha}^{\alpha+\gamma} \sin(m\theta) \cos(n\theta) \mathrm{d}\theta; & I_{nm}^{(8)} = \int_{\alpha}^{\alpha+\gamma} \sin(m\theta) \sin(n\theta) \mathrm{d}\theta \end{cases} \tag{21}$$

The unknown complex coefficients A_n, B_n, C_n, and D_n are obtained explicitly by solving Equations (12), (13), (19), and (20). Optimal convergence can be achieved after finite terms are applied to the expansion series. After gaining the unknown complex coefficients, the velocity potentials in the two sub-regions can also be easily acquired. According to the known velocity potential, the free-surface wave elevation may be calculated as follows:

$$\eta^{(j)} = -\frac{1}{g}\frac{\partial \phi^{(j)}}{\partial t} \quad (z = h, j = 1, 2) \tag{22}$$

where

$$\eta^{(1)} = \frac{\omega H}{2\omega^*} e^{-i\omega t} \sum_{n=0}^{\infty} \Big\{ \epsilon_n J_n(kr)\cos(n\theta)\cos(n\chi) + H_n^{(1)}(kr)[A_n \cos(n\theta) + B_n \sin(n\theta)] \Big\} \tag{23}$$

$$\eta^{(2)} = \frac{\omega H}{2\omega^*} e^{-i\omega t} \sum_{n=0}^{\infty} \Big\{ C_n \cos(n\theta) + D_n \sin(n\theta)] \times [J_n(kr) - \frac{J_n'(kb)}{H_n^{(1)\prime}(kb)} H_n^{(1)}(kr)] \Big\} \tag{24}$$

The forces acting on the surface of the semi-enclosed and enclosed structures along the horizontal plane F_{1x}, F_{1y}, F_{2x} and F_{2y} in two orthogonal directions are calculated by integrating the pressure difference between the two sides. Hence, the wavefield pressure is distributed as follows:

$$P^{(j)} = -\rho \frac{\partial \phi^{(j)}}{\partial t} \text{ for } j = 1, 2 \tag{25}$$

Accordingly,

$$\begin{cases} F_{1x} = \int_0^h \mathrm{d}z \int_\alpha^{\alpha+\gamma} [P^{(1)} - P^{(2)}]|_{r=a} a \sin\alpha \mathrm{d}\theta = \mathrm{Re}(f_{1x}) \\ f_{1x} = -\frac{\rho g A a \omega}{\omega^*} \frac{\tanh kh}{kh} e^{-i\omega t} \sum_{n=0}^{\infty} [\epsilon_n J_n(ka) cos(n\chi) + A_n H_n^{(1)}(ka) - C_n J_n(ka)] I_{n1}^{(3)} \\ + [B_n H_n^{(1)}(ka) - D_n J_n(ka)] I_{n1}^{(4)} \\ F_{1y} = -\int_0^h \mathrm{d}z \int_\alpha^{\alpha+\gamma} [P^{(1)} - P^{(2)}]|_{r=a} a \cos\alpha \mathrm{d}\theta = \mathrm{Re}(f_{1y}) \\ f_{1y} = -\frac{\rho g A a \omega}{\omega^*} \frac{\tanh kh}{kh} e^{-i\omega t} \sum_{n=0}^{\infty} [\epsilon_n J_n(ka) cos(n\chi) + A_n H_n^{(1)}(ka) - C_n J_n(ka)] I_{n1}^{(7)} \\ + [B_n H_n^{(1)}(ka) - D_n J_n(ka)] I_{n1}^{(8)} \end{cases} \tag{26}$$

$$\begin{cases} F_{1x} = \int_0^h \mathrm{d}z \int_0^{2\pi} P^{(2)}|_{r=b} b \sin\alpha \mathrm{d}\theta = \mathrm{Re}(f_{1x}), f_{1x} = -\frac{\rho g A a \omega}{\omega^*} \frac{\tanh kh}{kh} e^{-i\omega t} C_1 J_1(ka) \\ F_{1y} = -\int_0^h \mathrm{d}z \int_0^{2\pi} P^{(2)}|_{r=b} b \cos\alpha \mathrm{d}\theta = \mathrm{Re}(f_{1y}), f_{1y} = -\frac{\rho g A a \omega}{\omega^*} \frac{\tanh kh}{kh} e^{-i\omega t} D_1 J_1(ka) \end{cases} \tag{27}$$

Therefore, the total hydrodynamic loads acting on the arc wall and cylinder are given by:

$$F_{arc} = \sqrt{F_{x1}^2 + F_{y1}^2}, F_{cyl} = \sqrt{F_{x2}^2 + F_{y2}^2} \tag{28}$$

Furthermore, the maximum dimensionless total force acting on the arc wall and cylinder are defined as follows:

$$F_{arc}^{max} = \frac{F}{\rho g H a h}; F_{cyl}^{max} = \frac{F}{\rho g H a h} \tag{29}$$

In addition, wave propagation is characterized by the total force per unit height [1,26]

$$\begin{aligned}\frac{\mathrm{d}F_x}{\mathrm{d}z} &= -R\int_0^{2\pi} p\cdot\cos(\theta)\mathrm{d}\theta \\ &= P\left(k_x,k_y,k,R\right)\cdot\rho gAR\cdot\frac{\cosh(kz)}{\cosh(kh)}\mathrm{e}^{-\mathrm{i}\omega t},\end{aligned} \tag{30}$$

where the function $P(k_x,k_y,k,R)$ is a function solely related to the unknown coefficients, and R denotes the radii of the exterior and interior structures (a or b).

3. Model Validation

To validate the present analytical results, the results obtained by Jian et al. [29], Song and Tao [1], and Liu et al. [26] were compared with our results when the short-crested wave interacted with the same structures accompanied, respectively.

(1) When the opening angle is at $\gamma = 0$, the present structure can be regarded as a solid cylinder. We considered the concentric structure with parameter values $h = 5$ m, $\beta = \pi/6$, $b = 1$ m, $\gamma = 0$, and $U_0 = 0.2$ m/s. Figure 2 shows the non-dimensional wave run-up around the solid cylinder between the present results and the analytical results of Jian et al. [29], from which an excellent agreement can be observed.

(2) When the opening angle is at $\gamma = 2\pi$, the present structure can be regarded as a concentric dual-cylinder structure, and the uniform current speed is set to $U_0 = 0$, that is, the entire flow field can be considered as no uniform current. We considered the concentric structure with parameter values $a = 2$ m, $b = 1$ m , $h/a = 1$, $k_x = k_y = \sqrt{2}/2$, $U_0 = 0$, $G = 1$, $\gamma = \pi$ and $k_x/k = \sqrt{2}/2$. Figure 3 demonstrates an optimal agreement of the non-dimensional force on the two cylinders for the present results and the analytical results of Song and Tao [1].

(3) When the uniform current velocity is set to $U_0 = 0$, the whole flow field has no uniform current. We considered the concentric structure with parameter values $a = 2$ m, $b = 1$ m , $h/a = 1$, $k_x = k_y = \sqrt{2}/2$, $U_0 = 0$, $G = 1$, $\gamma = \pi$ and $k_x/k = \sqrt{2}/2$. Figure 4 illustrates that the non-dimensional wave surface around the concentric structure agrees well with the numerical results of Liu et al. [26]. Hence, this validates that our model is accurate and reliable.

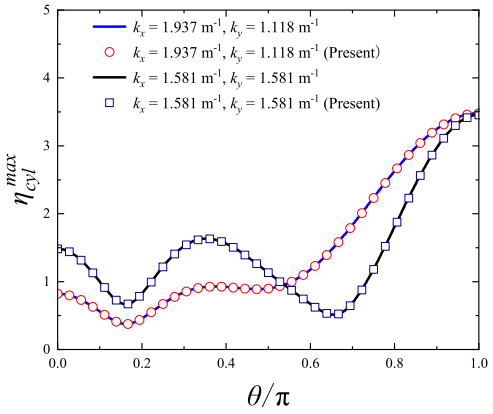

Figure 2. The non-dimensional wave run-up around a solid cylinder obtained from the present model was compared with the results from Jian et al. [29] (plotted as lines) with $h = 5$ m, $\beta = \pi/6$, $b = 1$ m, $\gamma = 0$, and $U_0 = 0.2$ m/s.

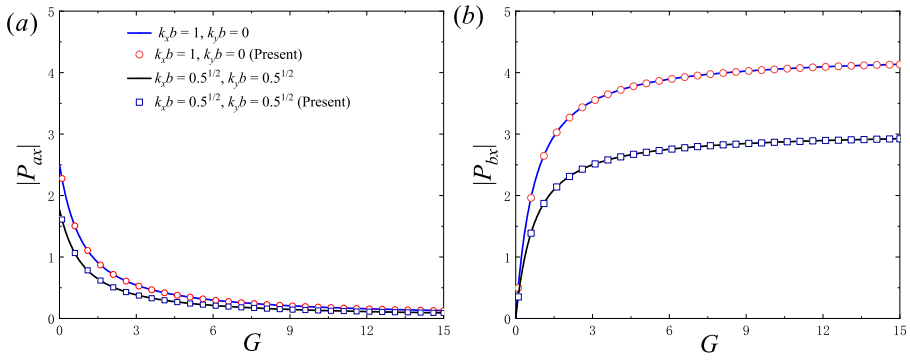

Figure 3. The non-dimensional wave force on a concentric cylindrical system obtained from the present model was compared with the results from Song and Tao [1] (plotted as lines) with $a = 4$ m, $b = 1$ m, $h/a = 1$, $kb = 1$, $\gamma = 2\pi$, $k_x/k = 1$, and $U_0 = 0$: (**a**) exterior cylinder; (**b**) interior cylinder.

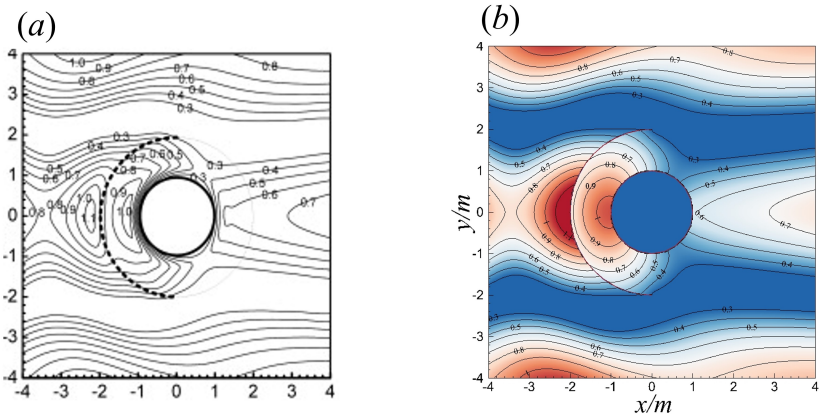

Figure 4. Comparison of the dimensionless wave surface distribution with $a = 2$ m, $b = 1$ m, $h/a = 1$, $k_x = k_y = \sqrt{2}/2$, $U_0 = 0$, $G = 1$, $\gamma = \pi$, and $k_x/k = \sqrt{2}/2$: (**a**) numerical results [26]; (**b**) analytical results (present).

4. Numerical Results and Discussions

A numerical procedure was developed to realize the obtained analytical solution and investigate the effect of different factors for short-crested wave scattering from the concentric structure. Let us consider the wave height $H = 2$ m. The radius of the arc wall and the water depth are set to $a = h = 4$ m.

4.1. Effects of the Current Velocity

Figure 5 demonstrates the wave load acting on the interior cylinder against ka for different U_0 and $|\beta - \chi|$ with $a/b = 2$, $a/h = 1$, $k_x/k = 0.5$, $\beta = \pi/3$, $G = 1$, $\alpha = 2\pi/3$, and $\gamma = 2\pi/3$. Figure 5 demonstrates that the force peaked at small wavenumbers and then decreased gradually, without depending on the current velocity. As expected, the force significantly increased (decreased) as U_0 increased when the direction of the uniform current was parallel to the identical (opposite) direction of wave propagation. Furthermore, for $U_0 = 1.2$ m/s, the peak forces were about 1.35 ($|\beta - \chi| = 0$) and 0.92 ($|\beta - \chi| = \pi$). Compared to the maximum value of 1.09 for the no-current case, the forces increased and decreased by approximately 22% and 15%, respectively. Figure 6 presents the run-up around the interior cylinder against θ/π for different U_0 and $|\beta - \chi|$ values with $ka = 4$, $a/b = 2$, $a/h = 1$, $k_x/k = 0.5$, $G = 1$, $\beta = \pi/3$, $\alpha = 2\pi/3$, and $\gamma = 2\pi/3$. In Figure 5, the run-up presented a similar tendency as the wave force, that is, the current velocity significantly influenced the wave run-up.

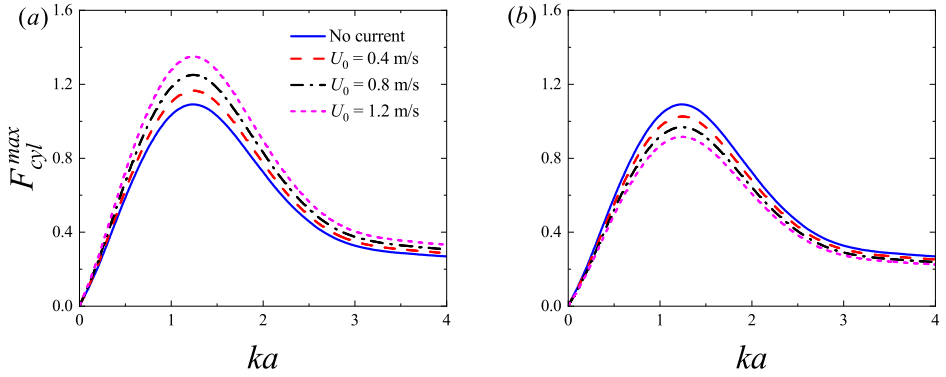

Figure 5. Variation of non-dimensional total wave force on the interior cylinder for different currrent speeds U_0 with $a/b = 2$, $a/h = 1$, $k_x/k = 0.5$, $\beta = \pi/3$, $G = 1$, $\alpha = 2\pi/3$, and $\gamma = 2\pi/3$: (**a**) $|\beta - \chi| = 0$; (**b**) $|\beta - \chi| = \pi$.

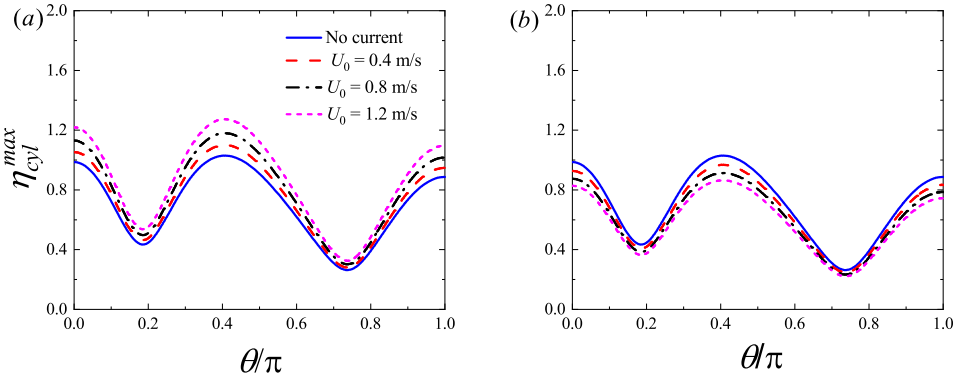

Figure 6. Variation of non-dimensional wave run-up on the interior cylinder for different currrent velocity U_0 with $ka = 4$, $a/b = 2$, $a/h = 1$, $k_x/k = 0.5$, $G = 1$, $\beta = \pi/3$, $\alpha = 2\pi/3$, and $\gamma = 2\pi/3$: (**a**) $|\beta - \chi| = 0$; (**b**) $|\beta - \chi| = \pi$.

Figure 7 shows the wave load and run-up on the interior cylinder for different values of β with parameter values $a/b = 2$, $a/h = 1$, $k_x/k = 0.5$, $G = 1$, $\beta = \pi/3$, $\alpha = 2\pi/3$, and $\gamma = 2\pi/3$: (a) force; (b) run-up, $ka = 4$. As $|\beta - \chi| < \pi/2$ ($|\beta - \chi| > \pi/2$), the force and run-up by the wave–current were smaller (larger) than those by the wave alone. The uniform current did not influence the force and run-up as $|\beta - \chi| = \pi/2$ (the wave and current direction are orthogonal). Mathematically, the existence of uniform current in the flow domain mainly alters the wave frequency of the entire flow field. When $|\beta - \chi| = \pi/2$, the uniform current hardly influenced the wave frequency; therefore, the force and run-up was also unaffected.

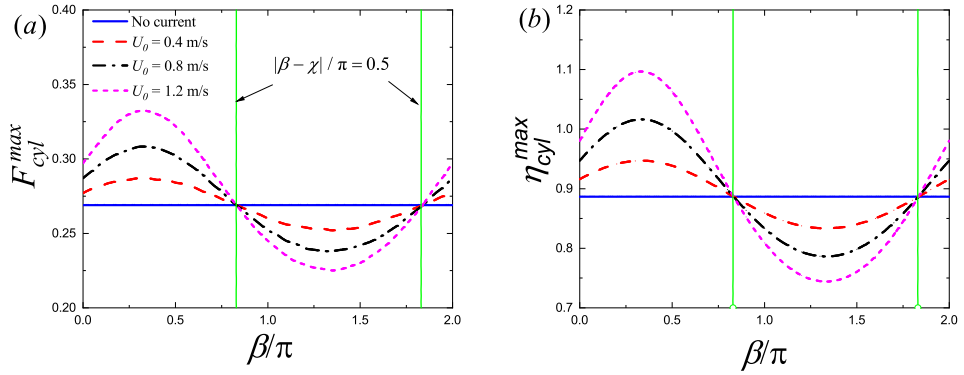

Figure 7. Variation in non-dimensional total wave force and run-up on the interior cylinder for different current speeds U_0 with $a/b = 2$, $a/h = 1$, $k_x/k = 0.5$, $\beta = \pi/3$, $G = 1$, $\alpha = 2\pi/3$, and $\gamma = 2\pi/3$: (**a**) wave force; (**b**) wave run-up, $ka = 4$.

4.2. Influence of Radius Ratio b/a

Figure 8 illustrates the hydrodynamic loads on the concentric structure corresponding to various k_x/k with parameter values $ka = 4$, $h/a = 1$, $\beta = \pi/3$, $U_0 = 0.4$ m/s, $G = 1$, $\alpha = 2\pi/3$, and $\gamma = 2\pi/3$: (a) arc wall; (b) interior cylinder. Form Figure 8, the hydrodynamic load acting on the concentric structure decreased gradually as $k_x/k = 1 \rightarrow 0$, that is, the largest wave loads corresponding to plane wave ($k_x/k = 1$) and the smallest wave loads corresponding to standing wave ($k_x/k = 0$). In other words, the best option is to adopt a plane wave model and estimate the wave loads on structures in the water domain of short-peaked waves; however, this is also relatively expensive to construct. In addition, the wave load on the cylinder is closely related to the annular spacing and the incident wave length. When the annular spacing is relatively large (b/a relatively small) and the incident wave length is relatively short (k relatively small), the force is relatively larger (see Figure 8b). For example, the peak value of the force on the cylinder occurs at approximately $b/a = 0.3$. The possible reasons are that long waves more easily round the structure and are transmitted to the annular region with a larger physical space to develop.

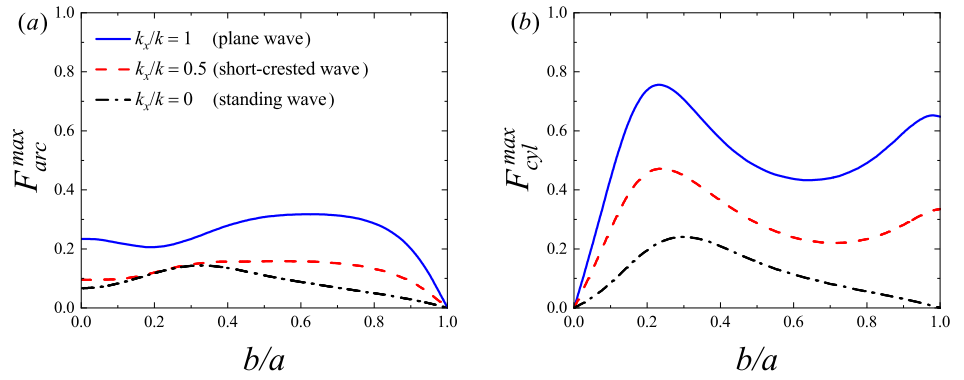

Figure 8. Variation in non-dimensional wave force on the two cylinders for different k_x/k with $ka = 4$, $h/a = 1$, $\beta = \pi/3$, $U_0 = 0.4$ m/s, $G = 1$, $\alpha = 2\pi/3$, and $\gamma = 2\pi/3$: (**a**) arc wall; (**b**) interior cylinder.

This concentric structure comprises closed cylindrical and semi-closed arc structures, which allows the arc wall to be a dense structure. Figure 9 presents the hydrodynamic force and run-up on the interior cylinder for different b/a with parameter values $\beta = \pi/3$, $h/a = 1$, $k_x/k = 0.5$, $U_0 = 0.4$ m/s, $G = 0$, $\alpha = 2\pi/3$, and $\gamma = 2\pi/3$: (a) force; (b) run-up, $ka = 1.4$. Figure 9a demonstrates that the force reached the maximum value in the vicinity of $ka = 1.4$. When the ratio $b/a > 0.7$, an abrupt increase in wave force occurred, which can be attributed to the resonance situation. In Figure 9b, with the ratio b/a increasing, on the windward side, the wave run-up gradually increased; when $b/a > 0.7$, the run-up increased steeply, which agrees well with the change in wave force. This illustrates that

under conditions $G = 0$, $ka = 1.4$, and $b/a > 0.7$, resonance will occur when the short-crested wave interacts with the concentric structure, and such situations should be avoided in practical engineering.

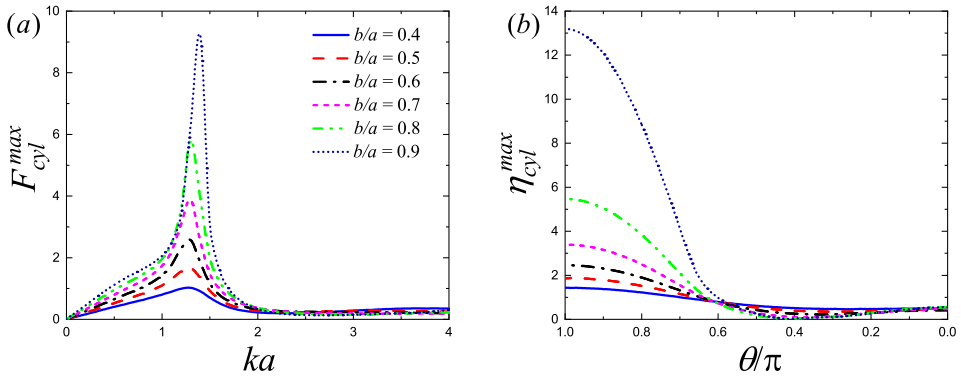

Figure 9. Variation in non-dimensional wave force and run-up on the interior cylinder for different b/a with $\beta = \pi/3$, $h/a = 1$, $k_x/k = 0.5$, $U_0 = 0.4$ m/s, $G = 0$, $\alpha = 2\pi/3$, and $\gamma = 2\pi/3$: (**a**) force; (**b**) run-up, $ka = 1.4$.

4.3. Influence of Opening Angle

Figure 10 shows the hydrodynamic load and wave run-up acting on the interior cylinder corresponding to different γ with parameter values $\beta = \pi/3$, $h/a = 1$, $k_x/k = 0.5$, $U_0 = 0.4$ m/s, $G = 1$, and $\alpha = \pi - \gamma/2$: (a) force; (b) run-up, $ka = 3$. Figure 10a demonstrates that a gradual decrease in force is experienced by the cylinder as γ goes up from 0 to π; however, the force does not always decrease consistently with increasing γ, such as $\gamma = 2\pi$. In Figure 10b, on the weather side, the run-up decreases significantly when the cylinder is protected by the arc wall, whereas on the lee side, the run-up does not decrease significantly. By comparing the wave load and run-up on the interior cylinder, we observe that the arc structure adopted to replace the concentric dual-cylinder system ($\gamma = 2\pi$), such as $\gamma = 2\pi/3$ or π, has certain engineering application value. To improve the visual comparison of the protection effect of semi-closed arc and closed circular wall ($\gamma = 2\pi$) on the interior cylinder, Figure 11 presents the wave elevation at the free surface near the concentric structure for different γ with $ka = 3$, $\beta = \pi/3$, $h/a = 1$, $k_x/k = 0.5$, $U_0 = 0.4$ m/s, $G = 1$, and $\alpha = \pi - \gamma/2$: (a) $\gamma = 2\pi/3$; (b) $\gamma = \pi$; (c) $\gamma = 2\pi$. By comparing the three subplots, the diffracted wave pattern distribution of the interior cylinder on the windward side is closely similar. This also demonstrates that employing an arc wall to protect the interior cylinder is feasible.

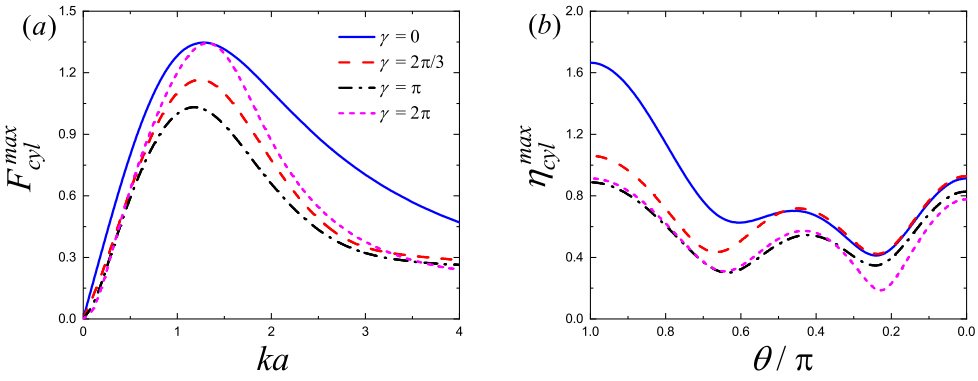

Figure 10. Variation in non-dimensional wave force and run-up on the interior cylinder for different values of γ with $\beta = \pi/3$, $h/a = 1$, $k_x/k = 0.5$, $U_0 = 0.4$ m/s, $G = 1$, and $\alpha = \pi - \gamma/2$: (**a**) force; (**b**) run-up, $ka = 3$.

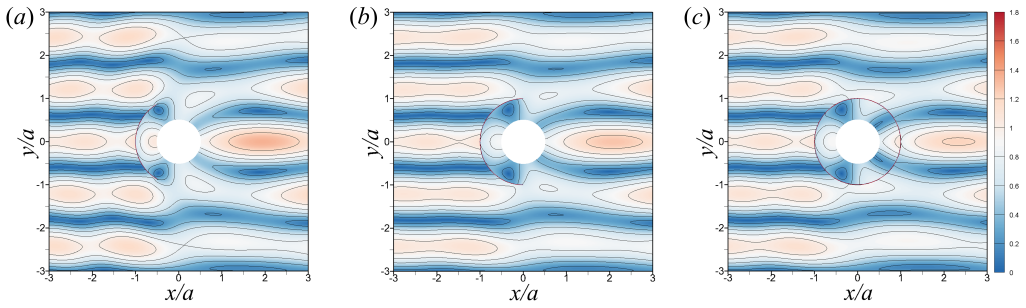

Figure 11. Distribution of the relative wave height for different values of γ with $ka = 3$, $\beta = \pi/3$, $h/a = 1$, $k_x/k = 0.5$, $U_0 = 0.4$ m/s, $G = 1$, and $\alpha = \pi - \gamma/2$: (**a**) $\gamma = 2\pi/3$; (**b**) $\gamma = \pi$; (**c**) $\gamma = 2\pi$.

4.4. Influence of Wave Parameters

Figure 12 shows the hydrodynamic load acting on the arc wall and cylinder for different parameter $k_x a$ with $a/b = 2$, $a/h = 1$, $\beta = \pi/3$, $G = 1$, $U_0 = 0.4$ m/s, $\alpha = 2\pi/3$, and $\gamma = 2\pi/3$: (a) arc wall; (b) interior cylinder. As illustrated in Figure 12a, because the arc wall is permeable resulting in different $k_x a$, the role of the arc wall of the wave load changes are not significant with increasing short-crestedness k_y/k_x. However, in the interior cylinder, two types of various patterns can be observed in the wave force. For large $k_x a$ values ($k_x a = 0.8, 1.6$), a significant decrease in the wave force acting on the interior cylinder can be observed, particularly in the interval of short-crestedness k_y/k_x from 0 to 3. When $k_x a$ is relatively small, such as $k_x a = 0.2$, there is no significant change in the wave force amplitude. In other words, the force on the cylinder varies in a small range and is not significantly dependent on short-crestedness. The physical mechanism of this alteration is as follows: The radius of the arc a is fixed, and a small $k_x a$ values implies a small k_x. As the short-crestedness k_y/k_x increases, the total wave number increases while the values of k_x/k decrease, that is, the short-crested waveform gradually approaches the standing wave (the general tendency of wave force is to decrease). In addition, the peak of the wave force corresponds to a total wave number at $k = 0.35$ ($ka = 1.4$), which implies that $k_x a = 1.4$ and $k_y/k_x = 0$ has a peak value. This critical characteristic of wave forces may be meaningfully incorporated into engineering applications to minimize the influence of waves on offshore and marine structures.

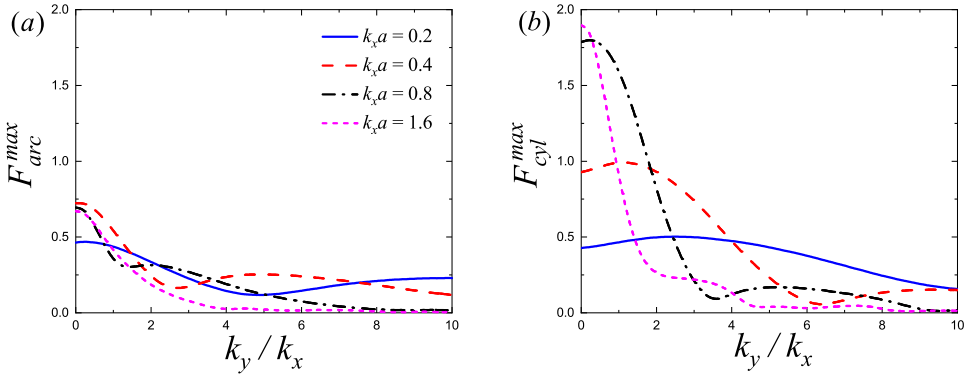

Figure 12. Variation of non-dimensional wave force on the arc wall and interior cylinder for different $k_x a$ values with $a/b = 2$, $a/h = 1$, $\beta = \pi/3$, $G = 1$, $U_0 = 0.4$ m/s, $\alpha = 2\pi/3$, and $\gamma = 2\pi/3$: (**a**) arc wall; (**b**) interior cylinder.

4.5. Influence of Location of the Outer Wall

Unlike regular waves such as the Airy wave, a short-crested wave is a superposition wave; hence, modifying the angle of incidence essentially alters the short-crestedness on the wave. However, we can complete the study of the interaction of obliquely incident waves with semi-enclosed structures by modifying the position of the structures. Figure 13 presents the hydrodynamic force on the cylinder against ka for different values of α with

$a/b = 2$, $a/h = 1$, $\beta = \pi/3$, $G = 1$, $U_0 = 0.4$ m/s, $\alpha = 2\pi/3$, and $\gamma = 2\pi/3$: (a) $k_x/k = 1$; (b) $k_x/k = 0.5$. From Figure 13, the hydrodynamic load on the cylinder increases gradually with increasing α. Because, as α decreases from $2\pi/3$ to $-\pi/3$, a rotation of the arc wall is conducted from being placed symmetrically around the negative half-axis of the x-axis to the positive half-axis, and the protective effect of the arc on the cylinder gradually decreases. For the plane wave (see Figure 13a), as the diffraction parameter ka increases, the hydrodynamic load on the cylinder follows a similar tendency to that of the single cylinder when $\alpha = \pi/6$. Interestingly, the force on the interior cylinder is larger than that on the single cylinder when $\alpha < \pi/6$. Consequently, the arc wall blocks the movement of waves and enhances wave reflection, leading to an increase in the force on the interior cylinder. This is similar to the increase in the interior cylinder force in a concentric dual-cylinder system (see, Figure 9a).

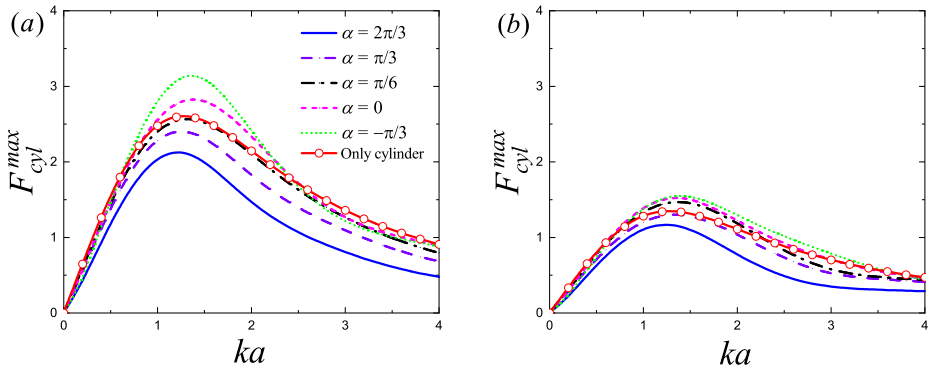

Figure 13. Variation in non-dimensional wave force on the interior cylinder for different α with $a/b = 2$, $a/h = 1$, $\beta = \pi/3$, $G = 1$, $U_0 = 0.4$ m/s, $\alpha = 2\pi/3$, and $\gamma = 2\pi/3$: (**a**) $k_x/k = 1$; (**b**) $k_x/k = 0.5$.

Figure 14 shows the wave elevation at the free surface near the concentric structure for different α with $ka = 2$, $a/h = 1$, $\beta = \pi/3$, $k_x/k = 0.5$, $G = 1$, $U_0 = 0.4$ m/s, and $\gamma = 2\pi/3$: (a) only cylinder; (b) $\alpha = 2\pi/3$; (c) $\alpha = \pi/3$; (d) $\alpha = \pi/6$; (e) $\alpha = 0$; (f) $\alpha = -\pi/3$. From Figure 14, when $-\pi/3 < \alpha < 2\pi/3$, that is, the arc wall is not placed symmetrically around the x-axis, the entire wave field loses symmetry characteristics of the y-axis and becomes more complex. Moreover, around the weather side, the water run-up on the interior cylinder enlarged obviously as α decreases. For $\alpha = -\pi/3$, around the weather side, the water run-up is slightly higher than that of the single cylinder. This is similar to the increasing tendency of wave force on the cylinder in Figure 13. In addition, compared to a concentric dual-cylinder system, this concentric structure consisting of a semi-closed arc-shaped structure and closed cylindrical structure is more sensitive to the wave incidence direction (or the location of the arc wall), that is, the concentric structure is more suitable for use in special sea areas such as relatively stable and less variable wave incidence directions.

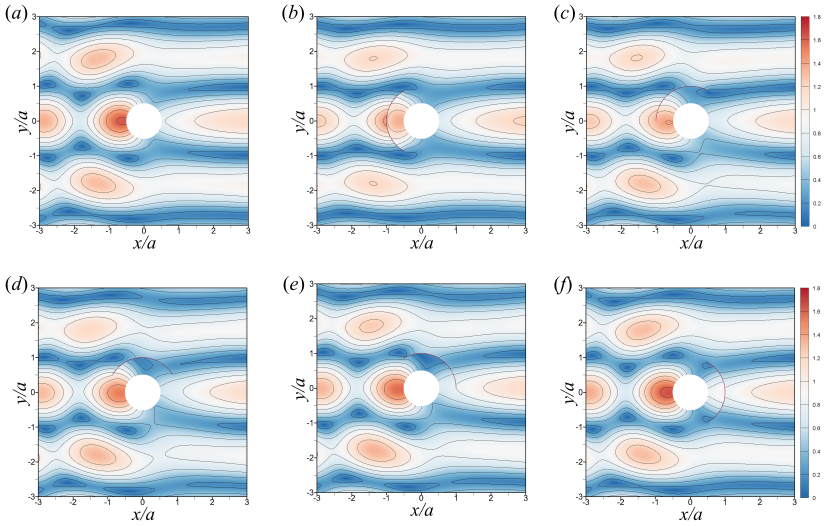

Figure 14. Distribution of the relative wave height for different values of α with $ka = 2$, $a/h = 1$, $\beta = \pi/3$, $k_x/k = 0.5$, $G = 1$, $U_0 = 0.4$ m/s, and $\gamma = 2\pi/3$: (**a**) only cylinder; (**b**) $\alpha = 2\pi/3$; (**c**) $\alpha = \pi/3$; (**d**) $\alpha = \pi/6$; (**e**) $\alpha = 0$; (**f**) $\alpha = -\pi/3$.

5. Conclusions

In this study, an analytical solution was derived to the diffraction problem for short-crested wave–current on a concentric structure comprising an arc exterior wall and an impermeable interior cylinder. By comparing the results of existing studies with the numerical calculations in this study, the validity of the present analytical solution is demonstrated. Several numerical experiments demonstrated the influence of various parameters, such as the current incident angle, current velocity, ratio of the radii of the exterior and interior structures, short-crestedness of the regular wave, and location of the arc wall, on hydrodynamic forces and wave run-up. Accordingly, the following conclusions are drawn:

(1) The wave incidence direction and the uniform inflow incidence direction have a significant effect on the wave force and run-up acting on the structure, that is, when the directions of them are the same ($|\beta - \chi| = 0$), the wave force and wave run-up acting on the cylinder and arc increases significantly, decreases significantly in the opposite condition ($|\beta - \chi| = \pi$), and has almost no effect when orthogonal ($|\beta - \chi| = \pi/2$).

(2) Under the condition of $G = 0$, $ka = 1.4$, and $b/a > 0.7$, a resonance phenomenon may occur when the short-crested wave–structure interaction occurs; the resonance phenomenon may be more pronounced owing to the presence of a uniform current accompanied with the wave–current in the same incident direction, which may significantly increase the risk of structural overturning.

(3) Considering that the short-crested wave is a special superposition state waveform, it is highly feasible to employ the present concentric structure as a replacement for the concentric dual-cylinder system in the corresponding waters, which can exert a sufficient protection effect, in addition to reducing the project cost.

(4) By studying the position of the arc wall, the semi-enclosed structure has certain limitations in engineering applications, (i.e., it is very sensitive to the wave incidence direction), which implies that the semi-enclosed structure has certain requirements for sea conditions. Future experimental studies can be conducted to verify the accuracy of the current analytical model and provide references for practical engineering applications.

Author Contributions: Conceptualization, Z.Z.; methodology, D.L.; validation, Z.Z. and J.L.; formal analysis, Z.Z. and J.M.; investigation, Z.Z. and J.M.; resources, D.L.; writing—original draft preparation, Z.Z. and J.M.; writing—review and editing, J.L. All authors have read and agreed to the published version of the manuscript.

Funding: This work is supported by the Special project for marine economy development of Guangdong Province (GDNRC [2021] 45) and (GDNRC [2022] 31), the Natural Science Foundation of China (42227901), Innovation Group Project of Southern Marine Science and Engineering Guangdong Laboratory (Zhuhai) (311020011), Key-Area Research and Development Program of Guangdong Province (2020B1111010004).

Institutional Review Board Statement: Not applicable.

Informed Consent Statement: Not applicable.

Data Availability Statement: All relevant data are within the paper.

Conflicts of Interest: The authors declare no conflict of interest.

References

1. Song, H.; Tao, L.B. Short-crested wave interaction with a concentric porous cylindrical structure. *Appl. Ocean Res.* **2007**, *29*, 199–209. [CrossRef]
2. Chwang, A.T. A porous-wavemaker theory. *J. Fluid Mech.* **1983**, *132*, 395–406. [CrossRef]
3. Chwang, A.T.; Li, W. A piston-type porous wavemaker theory. *J. Eng. Math.* **1983**, *17*, 301–313. [CrossRef]
4. Wang, K.H.; Ren, X.G. Wave interaction with a concentric porous cylinder system. *Ocean Eng.* **1994**, *21*, 343–360. [CrossRef]
5. Li, Y.C.; Sun, L.; Teng, B. Wave interaction with arrays of combined cylinders with and solid interior column and a porous exterior column. *Acta Mech. Sin.* **2005**, *37*, 141–147.
6. Teng, B.; Han, L.; Li, Y. Ware diffraction from a vertical cylinder with two uniform columns and porous outer wall. *China Ocean Eng.* **2000**, *14*, 297–306.
7. Vijayalakshmi, K.; Neelamani, S.; Sundaravadivelu, R.; Murali, K. Wave runup on a concentric twin perforated circular cylinder. *Ocean Eng.* **2007**, *34*, 327–336. [CrossRef]
8. Vijayalakshmi, K.; Sundaravadivelu, R.; Murali, K.; Neelamani, S. Hydrodynamics of a concentric twin perforated circular cylinder system. *J. Waterw. Port Coast. Ocean Eng.* **2008**, *134*, 166–177. [CrossRef]
9. Zhu, S.; Chwang, A.T. Investigations on the reflection behaviour of a slotted seawall. *Coast. Eng.* **2001**, *43*, 93–104. [CrossRef]
10. Tao, L.; Song, H.; Chakrabarti, S. Scaled boundary fem model for interaction of short-crested waves with a concentric porous cylindrical structure. *J. Waterw. Port Coast. Ocean Eng.* **2009**, *135*, 200–212. [CrossRef]
11. Zhai, Z.; Zhao, W.; Wan, D.; Liu, D. Interaction of solitary wave with a concentric structure with multiple porous outer walls. *Ocean Eng.* **2022**, *260*, 111887. [CrossRef]
12. Zhong, Z.; Wang, K.H. Solitary wave interaction with a concentric porous cylinder system. *Ocean Eng.* **2006**, *33*, 927–949. [CrossRef]
13. Sankarbabu, K.; Sannasiraj, S.A.; Sundar, V. Interaction of regular waves with a group of dual porous circular cylinders. *Appl. Ocean Res.* **2007**, *29*, 180–190. [CrossRef]
14. Zhao, Y.; Liu, Y.; Li, H. Wave interaction with a partially reflecting vertical wall protected by a submerged porous bar. *J. Ocean. Univ. China* **2016**, *15*, 619–626. [CrossRef]
15. Zhai, Z.; Li, H.; Zhang, A.; Song, A.;Wang, K. Analytical modelling of water wave diffraction by a bottom-mounted surface-piercing concentric dual-arc porous thin wall. *Ocean Eng.* **2021**, *236*, 109485. [CrossRef]
16. Zhai, Z.; Shao, Y.; Wang, K.; Huang, H.; Li, H. Semi-analytical solution of cnoidal wave diffraction around a double-layer arc-shaped vertical porous breakwater. *J. Fluids Struct.* **2021**, *103*, 103261. [CrossRef]
17. Zhai, Z.; Hu, Q.; Yang, L.; Huang, H. Diffraction of Solitary Waves by a Concentric Porous Dual-Arc Thin Wall. *J. Waterw. Port Coast. Ocean Eng.* **2022**, *148*, 04022001. [CrossRef]
18. Liu, J.; Guo, A.; Nandasena, N.; Melville, B.W.; Li, H. Theoretical and experimental investigation on wave interaction with a concentric porous cylinder form of breakwater. *Ocean Eng.* **2018**, *160*, 156–167. [CrossRef]
19. Sarkar, A.; Bora, S.N. Hydrodynamic forces and moments due to interaction of linear water waves with truncated partial-porous cylinders in finite depth. *J. Fluids Struct.* **2020**, *194*, 102898. [CrossRef]
20. Zheng, S.; Meylan, M.H.; Zhu, G.; Greaves, D.; Iglesias, G. Hydroelastic interaction between water waves and an array of circular floating porous elastic plates. *J. Fluid Mech.* **2020**, *900*, A20. [CrossRef]
21. Zheng, S.; Meylan, M.H.; Greaves, D.; Iglesias, G. Water-wave interaction with submerged porous elastic disks. *Phys. Fluids* **2020**, *32*, 047106.
22. Zheng, S.; Meylan, M.H.; Fan, L.; Greaves, D.; Iglesias, G. Wave scattering by a floating porous elastic plate of arbitrary shape: A semi-analytical study. *J. Fluids Struct.* **2020**, *92*, 102827. [CrossRef]
23. Cuong, D.Q.; Tuan, T.Q. Wave Hydrodynamics across Steep Platform Reefs: A Laboratory Study. *Civ. Eng. J.* **2022**, *8*, 1739–1751. [CrossRef]
24. Kamil, E.A.; Takaijudin, H.; Hashim, A.M. Mangroves as coastal bio-shield: A review of mangroves performance in wave attenuation. *Civ. Eng. J.* **2021**, *7*, 1964–1981. [CrossRef]
25. Zhu, S. Diffraction of short-crested waves around a circular cylinder. *Ocean Eng.* **1993**, *20*, 389–407. [CrossRef]

26. Liu, J.; Lin, G. Numerical modelling of wave interaction with a concentric cylindrical system with an arc-shaped porous outer cylinder. *Eur. J. Mech. B-Fluids* **2013**, *37*, 59–71. [CrossRef]
27. Zhai, Z.; Li, X.; Yang, L. Analytical approach to the solution of short-crested wave interaction with v-shaped and arc-shaped breakwaters. *Phys. Fluids.* **2022**, *34*, 022112. [CrossRef]
28. Lin, P.; Li, C.W. Wave–current interaction with a vertical square cylinder. *Ocean Eng.* **2003**, *30*, 855–876. [CrossRef]
29. Jian, Y.; Zhan, J.; Zhu, Q. Short crested wave–current forces around a large vertical circular cylinder. *Eur. J. Mech. B-Fluids* **2008**, *27*, 346–360. [CrossRef]
30. Wang, P.; Zhao, M.; Du, X. Short-crested wave–current forces on composite bucket foundation for an offshore wind turbine. *Math. Probl. Eng.* **2019**, *2019*, 5932742. [CrossRef]
31. Zhou, Y.; Zhou, E. Numerical simulation of wave–current interaction on submerged diketerrain. *Int. Core J. Eng.* **2021**, *7*, 173–180.
32. Huang, J.; Teng, B.; Cong, P. Wave–current interaction with three-dimensional bodies in a channel. *Ocean Eng.* **2022**, *249*, 110952. [CrossRef]
33. Zhou, X.; Jiang, Q.; Wang, Y.; Chen, L.; Wang, S.; Wang, K. Numerical Simulation of Wave–Current Force Characteristics of Horizontal Floating Cylinder in Heave Motion. *J. Mar. Sci. Eng.* **2022**, *10*, 1884. [CrossRef]